The Astrophysical Journal, 890:178 (11pp), 2020 February 20 https://doi.org/10.3847/1538-4357/ab612c

Water in the Star-forming Region NGC 7129 FIRS 2

Mollie E. Conrad and Michel Fich
Department of Physics & Astronomy, University of Waterloo, 200 University Avenue, Waterloo, ON, N2L 3G1, Canada; fich@uwaterloo.ca
Received 2018 October 12; revised 2019 December 7; accepted 2019 December 10; published 2020 February 26

Abstract

Observations of intermediate mass (IM) star formation are expected to highlight the transition between the formation processes of its low and high-mass (HM) counterparts. $H_2^{18}O$ and $H_2^{16}O$ observations of the IM star formation region NGC 7129 FIRS 2 were obtained with the Heterodyne Instrument for the Far-Infrared aboard the *Herschel Space Observatory*; most as part of the WISH key-program. The radiative transfer program RATRAN was used to model water emission from the envelope of this star-forming region. We consider the envelope in two regions, inner and outer envelope, which are separated by the water freeze-out radius. An outer envelope ortho-$H_2^{18}O/H_2$ abundance was determined to be $3.5 \pm 0.3 \times 10^{-11}$, and an outer turbulent velocity was determined to be $2.25 \pm 0.25\,\mathrm{km\,s^{-1}}$. The outer envelope ortho-$H_2^{16}O/H_2$ and para-$H_2^{16}O/H_2$ abundances were determined to be $1.5 \pm 0.5 \times 10^{-8}$ and $4.5 \pm 0.5 \times 10^{-9}$, respectively. The inner envelope abundances and turbulent velocity could not be constrained due to increased optical depth. The derived values are consistent with those found by low-mass (LM) and HM young stellar object studies of water. While the line shapes and intensities of these lines are more similar to the spectral lines found for LM objects, the turbulent velocity is closer to that seen in HM objects. Lastly, we present a simple visualization tool that we created to show that these abundance results, particularly the limited extent probed by these lines, should not have been a surprise. This tool can be very useful in planning future molecular line observations.

Unified Astronomy Thesaurus concepts: Interstellar abundances (832); Interstellar molecules (849); Astrochemistry (75); Star formation (1569)

1. Introduction

The formation process of isolated low-mass (LM) stars is well understood with an initial phase of spherical accretion onto a central protostar changing to a phase dominated by disk accretion (see, e.g., Shu & Adams 1987). Our understanding of the formation of high-mass (HM) stars is more limited. A fundamental problem in the formation of HM stars is that the central star forms so quickly in most models that the star will form and cut off the accretion process before the star accumulates much mass. LM stars form with high efficiencies and can incorporate over 50% of the prenatal dense core mass into a bound stellar cluster (e.g., Wilking & Lada 1983). HM star formation on the other hand, while occurring in much higher mass clouds such as Giant Molecular Clouds, typically include only a few percent of the cloud mass into the stars (e.g., Cohen & Kuhi 1979; Evans et al. 2009). Wolfire & Cassinelli (1987) showed that radiation pressure from $10\,M_\odot$ central stars would halt normal spherical accretion with gravity from a central star overcoming thermal supported envelopes. Since stars are known with masses up to nearly $100\,M_\odot$ a number of schemes were found to overcome this such as "core accretion" models with enhanced spherical accretion when the surrounding cloud is supported by turbulence and a massive centrally concentrated core is already collapsing before the central star is formed (McKee & Tan 2003). Nonspherical accretion models include "competitive accretion" where a protostar gains mass by Bondi–Hoyle accretion, sweeping up material as it moves through a large cloud (Bonnell et al. 2001). Although most HM star formation models include an accretion disk at some point in the process, the detection of such disks is rare with only a handful detected. Conversely, several hundred disks have been found so far around lower mass stars. The importance of disks in HM star formation is not yet known." A recent review is provided by Tan (2014).

Between the LM and HM stars there are stars of intermediate mass (IM) that may be observed to provide some insight into the mechanisms of higher mass star formation. Unfortunately there are few cataloged, nearby, young, IM protostars.

The WISH key-program (Water In Star-forming regions with *Herschel* (van Dishoeck et al. 2011)) of the *Herschel Space Observatory* (Pilbratt et al. 2010) identified six candidates as possible IM Young Stellar Objects (YSOs) that were near enough to be observable in water emission lines with the Heterodyne Instrument for the Far-Infrared (HIFI) instrument (de Graauw et al. 2010). For the purposes of this study, IM YSOs were defined as those with bolometric luminosities between 75 $L_\odot$ and 2×10^3 $L_\odot$.

Previous studies have suggested a smooth transition in formation processes from the LM to HM regime (Testi & Sargent 1998; Fuente et al. 2007; Neri et al. 2007; Crimier et al. 2010; Matuszak et al. 2015). The WISH team confirmed this smooth transition, pointing out that "the line profiles are remarkably similar," although the LM and the IM line emission is dominated by outflows (van Dishoeck et al. 2011). Broader components in the line profiles were assumed to be due to the outflows and shocks associated with them, and to shocks at the innermost edges of the (spherical) envelopes. The inner envelope abundances were not well constrained in large part because of confusion with these broad components. Narrower components were used to estimate water abundances in the outer envelopes. The LM and HM abundances were similar, while the one IM object reported on, NGC 7129 FIRS 2, gave a somewhat higher abundance of water in its outer envelope. In this paper we re-examine the results for NGC 7129 FIRS 2 in light of the final data set available from the HIFI mission and utilizing improved models of the water emission.

Table 1
NGC 7129 FIRS 2 Properties

Property	NGC 7129 FIRS 2
R.A. (h m s)	21 43 01.7
decl. (° ′ ″)	+66 03 23.6
V_{LSR} (km s^{-1})	−9.8
M_{env} ($M_\odot$)	50
L_{bol} ($L_\odot$)	430
d (pc)	1250
Outflow	B(+60, +60), R(+60, −60)
$r_{in,\ env}$ (au)	100
$r_{out,\ env}$ (au)	18,600
References	Fuente et al. (2005), Eiroa et al. (1998), Shevchenko & Yakubov (1989), Crimier et al. (2010)

NGC 7129 FIRS 2, possibly the youngest IM object known at present (Crimier et al. 2010), is located within a reflection nebula nested inside a complex and active molecular cloud (Hartigan & Lada 1985; Miranda et al. 1993). Table 1 presents source information for this IM YSO. NGC 7129 FIRS 2 has been determined to have bipolar outflows (Edwards & Snell 1983; Fuente et al. 2001) and is classified as an IM Class 0 protostar (Eiroa et al. 1998) with a luminosity of 500 $L_\odot$ and estimated stellar mass of 5 $M_\odot$ (Eiroa et al. 1998; Fuente et al. 2001, 2005). Fuente et al. (2005) presented the first detections of a hot core in NGC 7129 FIRS 2, the first detection in any IM YSO. Crimier et al. (2010) determined a density and temperature profile for a spherical envelope around NGC 7129 FIRS 2; the density was determined to vary with radius as a power law with index −1.4. Their best-fit model has an envelope mass of 50 $M_\odot$, with an inner radius of 100 au and an outer radius of 18,600 au. The temperature at the inner radius is 288.5 K, falling to 15.8 K at the outermost radius.

Johnstone et al. (2010) used the one-dimensional radiative transfer code RATRAN (Hogerheijde & van der Tak 2000) with Green et al. (1993) H_2O–He collisional cross sections (scaled by 1.348 for collisions with H_2) to model the ortho-$H_2^{16}O$ and $H_2^{18}O$ emission observed with HIFI. They assumed an H_2 ortho-to-para ratio (OPR) of 3, the Crimier et al. $p = 1.4$ profile, a freeze-out temperature of 100 K, and an abundance ratio of $H_2^{16}O/H_2^{18}O = 550$. Their best-fitting model parameters were turbulent velocity of $b = 2\ \mathrm{km\ s^{-1}}$ (where for a Gaussian line profile, $b/\mathrm{FWHM} = 1/2\sqrt{\ln 2} = 0.60$), an infall radial velocity of $v_r = \sqrt{2GM_*/R}$ where $M_* = 1.1M_\odot$, and an outer envelope ortho-$H_2^{18}O$ abundance of $3 \pm 1 \times 10^{-10}$, relative to H_2. These authors were also unable to place constraints on the inner envelope parameters.

In this current paper we build on the earlier work on NGC 7129 FIRS 2, especially that of Johnstone et al. (2010). That work used preliminary data from HIFI and included four $H_2^{16}O$ lines and two $H_2^{18}O$, all reduced using an early version of the data reduction pipeline (Herschel Interactive Processing Environment (HIPE) 3.0 versus HIPE 15.0.0) and the initial calibration data. Here we add two additional $H_2^{16}O$ lines and one additional $H_2^{18}O$ line, and we apply the mission final calibrations and pipeline. Previous work on this object only considered a few dozen models that varied the abundances in the inner and outer envelopes by combinations in factors of three and only coarsely sampled a range in turbulent velocity. In this current work we ran over 320 models; details on the model parameters can be found in Table 4.

2. Observations

This study uses data found in the archives of the *Herschel* mission. These data include spectra obtained under the WISH key-program and from later observations under *Herschel* Open Time and Guaranteed Time (Proposal ID: KPGT_evandish_1, Principal Investigator: Ewine van Dishoeck; van Dishoeck et al. 2011) available to one of us (MF) as a *Herschel*/HIFI Lead co-Investigator. The majority of the NGC 7129 FIRS 2 water observations were obtained in DBS observing mode, while the $H_2^{16}O$ ground state 557 GHz line was obtained using load chop. The water observation details are outlined in Table 2; the column titled "line" contains the line identifiers that appear in the RATRAN data files, which are also used in this paper.

The water observations used in this work are the level 2.0 calibrated data products (Roelfsema et al. 2012), which are prepared for scientific analysis (Ott 2010). These data products still require sub-band spectral stitching and baseline removal.

Using preliminary data and calibrations, Johnstone et al. 2010 also investigate the majority of the water lines studied in this work; this work expands on theirs by also including the ground-state ortho-$H_2^{16}O$ 557 GHz line, the excited state ortho-$H_2^{16}O$ 1153 GHz line, and the $H_2^{18}O$ excited 1095 GHz line.

2.1. Data Processing with HIPE

The HIPE (Ott 2010) version 15.0.0 was used to obtain the observations which included correcting (removal) for strong contaminating lines in some associated sub-bands of the data, "stitching" together side-bands, removing first-order baselines, and decomposing the observations into Gaussians. The processed observations are given in Figure 1 ($H_2^{16}O$) and Figure 2 ($H_2^{18}O$). The ortho and para ground-state line residuals show the absorption features that we did not attempt to fit; we attribute these to possible foreground clouds.

The separation into Gaussian components is needed as the lines are complex with contributions to the observed emission from a variety of sources. Some of the sources may produce double-peaked or extremely asymmetric lines that are poorly represented by a set of Gaussians but this decomposition provides a starting point for later analysis. Primarily this process selects the amount of emission to be included in the fits in the procedure discussed below. This is done because our interest is in the structure of the protostellar envelope where most of the mass resides and our models should only be fitted to the emission appropriate to that structure. The number of Gaussian components selected was based on an overview of the entire set of the observed line profiles and on the features expected in such star-forming regions: an envelope, a bipolar outflow, and possibly a hot core. Other features in these spectra include a deep absorption seen only in the ground-state lines of $H_2^{16}O$ and a narrow emission feature that is only clearly seen in the ground-state line of $H_2^{18}O$.

Following the lead of earlier investigators (e.g., Johnstone et al. 2010), we assume that the absorption feature is due to the larger cloud around the YSO core. It is very narrow (FWHM 2 km s^{-1}), centered at the velocity of the larger cloud (Font et al. 2001, Figure 3: FIRS 2 object at −30″, −100″), and

Table 2
Herschel HIFI Water Observations

Molecule	Transition	Line	OBSID	ν (GHz)	E_{up} (K)	Band	Integration Time (s)	Resolution (MHz)	Date	θ_{beam} ($''$)
$H_2^{16}O$	1_{10}–1_{01}	o-001	1342198329	556.936	61.0	1a	405	1.022	15 Jun 10	38.074
	1_{11}–0_{00}	p-001	1342191676	1113.343	53.4	4b	2431	1.135	05 Mar 10	19.046
	2_{02}–1_{11}	p-002	1342191613	987.927	100.8	4a	1271	1.022	03 Mar 10	21.464
	2_{11}–2_{02}	p-004	1342191747	752.033	136.9	2b	922	1.139	07 Mar 10	28.197
	3_{12}–2_{21}	o-006	1342198347	1153.127	249.4	5a	598	1.020	15 Jun 10	18.389
	3_{12}–3_{03}	o-007	1342191677	1097.365	249.4	4b	1803	1.018	05 Mar 10	19.323
$H_2^{18}O$	1_{10}–1_{01}	o-001	1342192362	547.676	61.0	1a	3599	1.139	20 Mar 10	38.718
	2_{02}–1_{11}	p-002	1342191614	994.675	100.8	4a	2265	1.022	03 Mar 10	21.318
	3_{12}–3_{03}	o-007	1342227393	1095.627	249.4	4b	6495	1.119	25 Aug 11	19.354

Note. o = ortho-water, p = para-water.

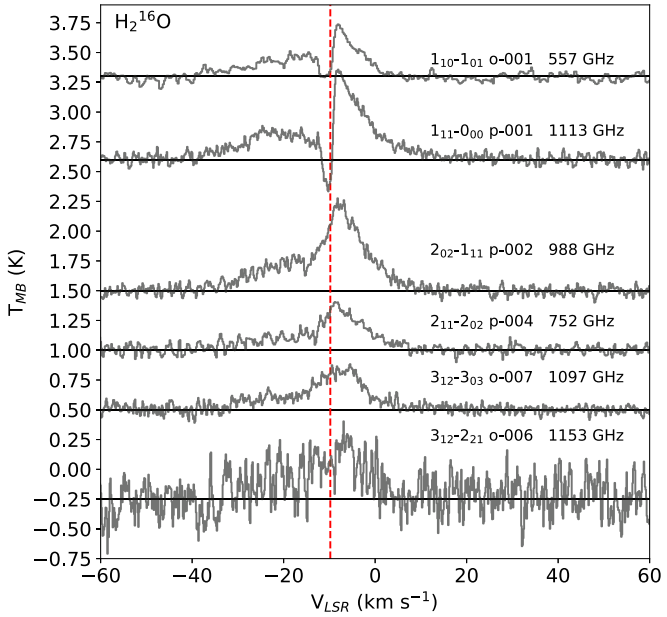

Figure 1. NGC 7129 FIRS 2 $H_2^{16}O$ Observations. System V_{LSR} located at -9.8 km s^{-1} (red dashed line).

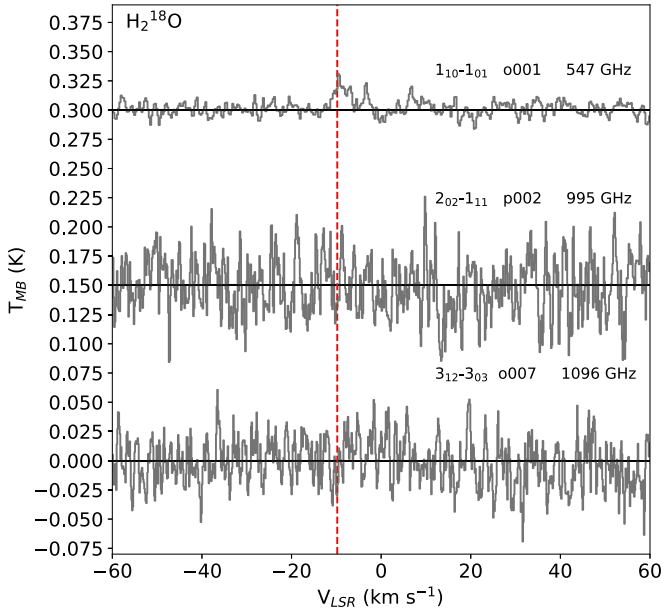

Figure 2. NGC 7129 FIRS 2 $H_2^{18}O$ Observations. System V_{LSR} located at -9.8 km s^{-1} (red dashed line).

not seen in any of the other lines, suggesting that it is quite cold. This absorption was not fit with a Gaussian.

The last feature (the "narrow emission") was also seen in the earlier work of Johnstone et al. (2010) but not discussed there; it was believed to be a foreground cloud since it is quite narrow and at a significantly different velocity from the target object. However, we do include this feature in our Gaussian fitting as it may contribute emission to some of the $H_2^{16}O$ lines observed and we wish to remove this contamination of the envelope emission.

HIPE optimizes the fits of a user-defined number of Gaussians in terms of width (km s^{-1}), amplitude (K), center (local standard of rest, V_{LSR}, km s^{-1}), and full-width half-max (FWHM, km s^{-1}). We chose to fix the V_{LSR} of all higher state line Gaussian components based on the optimized values given for the ground-state lines, while letting the other parameters vary. This choice was not strictly necessary but was done for several reasons. When wholly unconstrained, the Gaussian decomposition could in some cases give widely varying values, inconsistent with results found in measurements of the same component in a different line. Also, by fixing the line centers the model fitting procedure (below) was greatly simplified. Lastly, the fitting using the Gaussians is only the first step in the modeling of the envelopes and a greater level of accuracy was not particularly useful.

The Gaussian parameters can be found listed in Table 3, and the $H_2^{16}O$ and $H_2^{18}O$ Gaussian fits are plotted against the observations in Figures 3 and 4, respectively. We have selected three components for fitting: a very broad component ($\Delta V = >15$ km s^{-1}) that we associate with the outflow and the hot core, a component at a velocity of -7.7 km s^{-1} in the $H_2^{16}O$ that we associate with the envelope component, and a component at -3.4 km s^{-1} in the $H_2^{18}O$ that we associate with a foreground feature. In all of the $H_2^{16}O$ lines the outflow component is at least equal to and often dominates the emission from the other components. This highlights why removing this emission is important for the modeling of the envelope emission. This component was well fit by the Gaussian routine with little change in the values fitted as the inputs to the routine were changed.

In contrast, the fitting of the envelope and foreground feature was sensitive to the input velocity with significant variations in

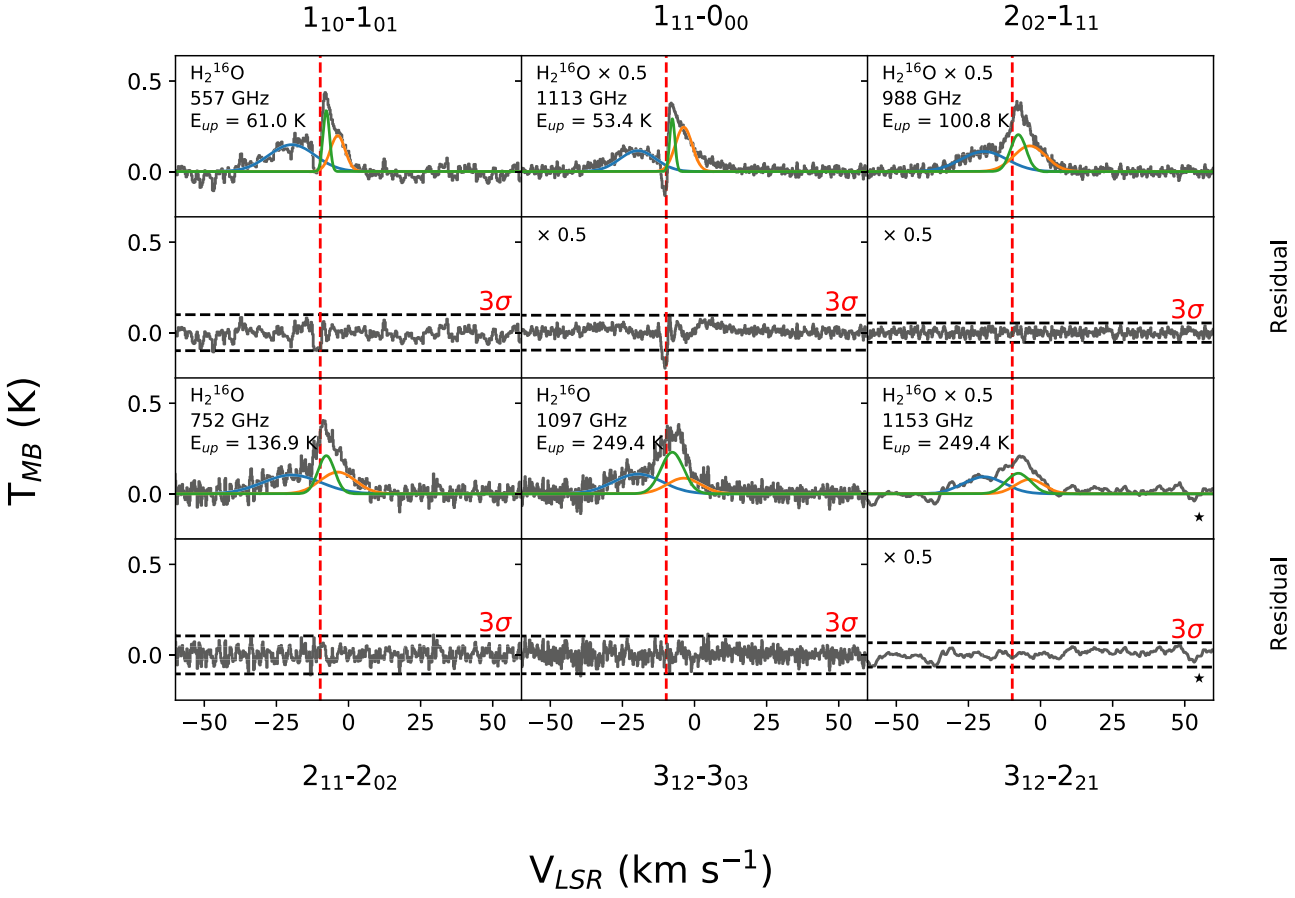

Figure 3. NGC 7129 FIRS 2: $H_2^{16}O$ Gaussian fits contrasted with $H_2^{16}O$ HIFI data. Medium feature located at -19.7 km s^{-1} (blue), narrow feature at -3.6 km s^{-1} (orange), and second medium feature at -7.8 km s^{-1} (green). The total fit is outlined in black. Gaussians are fit at the same position in each transition, but at varying widths. See Table 3 for further details. Local $V_{LSR} = -9.8$ km s^{-1}. Gaussian fits are subtracted from the HIFI data, yielding the residuals in the bottom panels. The 3σ boundaries around the residuals represent the goodness of fit of the Gaussians. The majority of fits are well encased by these boundaries; the para and ortho ground-state lines appear to have some unfitted features. The absorptions seen in this data were not fit. Some lines are scaled by 0.5: p001, p002, and o006.

all of the fitted parameters. As mentioned above, this was greatly alleviated by fixing the velocity of the line center but it can be seen that the line widths (FWHM) varied by a considerable amount (e.g., for the envelope component from 2.6 to 9.9 km s^{-1} and from 6.0 to 14.4 km s^{-1} for the foreground component. Of course, the emission line profiles are not likely to be Gaussian in nature for many of these lines and the line profiles for different lines will differ. A sign of the deviation from Gaussianity is that the integrated lines, if Gaussian, will be close to the product of T_{MB} and the FWHM and, while true for some components for some lines, this is often not the case.

The foreground feature appeared as a small but significant increase in emission on the positive velocity side of all of the $H_2^{16}O$ but was better fit at a velocity of -3.7 km s^{-1} in all cases. Also, in all of the fits of this component to the $H_2^{16}O$, the line width (FWHM) was much greater than in the $H_2^{18}O$ spectrum where it is most clearly seen.

In comparison with Johnstone et al. (2010), we observe slight differences between our Gaussian fits and theirs. They do not fit Gaussians to the ground-state para line. While we fit three Gaussians to our data, Johnstone et al. fit only two (narrow and broad). Because of this, our velocity integrated intensities specific to each component vary from theirs. The narrow components see a difference of 20%–25% while the broad components see a difference of up to 100% (para 2_{02}–1_{11}). Additionally, upon first glance, our $H_2^{16}O$ data generally have higher rms noise measurements (nearly double to triple their values); Johnstone et al. took their measurements over a much smaller velocity interval of 1 km s^{-1} compared to our interval of 120 km s^{-1} (-60 to $+60$ km s^{-1}). Even with the large difference in velocity range, our $H_2^{18}O$ rms noise measurements are consistent with Johnstone et al. ($\sim$5 km s^{-1}).

3. RATRAN Modeling

The 1D Monte Carlo radiative transfer code RATRAN (Hogerheijde & van der Tak 2000) was developed to model the line spectra of the dense and cool interstellar medium via rotational radiative transfer and molecular excitation calculations. Ossenkopf & Henning (1994) Jena dust models (henceforth referred to as "O&H") are used within RATRAN to consider the infrared field due to dust; the default model used by RATRAN is "jena,thin,e6," corresponding to thin mantles and 10^6 yr of coagulation. This code is only capable of modeling spherical molecular clouds—the outflow is not taken into consideration. As such, models produced by RATRAN can be compared to the envelope contribution of an observed spectral line (usually in the form of a Gaussian spectral fit). Deductions about the physical parameters of the envelope can be made from a best-fit model; if a single model fits multiple radiative transitions of a molecule or two, in this case $H_2^{16}O$ and

Table 3
Gaussian Fits to Spectral Line Emission

Transition	σ_{RMS} (mK)	Color in Figures 3 and 4	Component	V_{LSR} (km s^{-1})	T_{MB} (K)	$\int T_{MB} dv$ (K km s^{-1})	FWHM (km s^{-1})
o-$H_2^{16}O$	32.8	Blue	Outflow	−19.7	0.15 ± 0.006	3.0 ± 0.20	18.9 ± 1.1
1_{10}–1_{01}		Green	Envelope	−7.7	0.3 ± 0.030	0.9 ± 0.10	2.6 ± 0.2
		Orange	Foreground	−3.7	0.2 ± 0.020	1.3 ± 0.20	6.0 ± 0.8
p-$H_2^{16}O$	35.9	Blue	Outflow	−19.7	0.2 ± 0.007	3.6 ± 0.20	14.7 ± 0.5
1_{11}–0_{00}		Green	Envelope	−7.7	0.6 ± 0.020	1.3 ± 0.06	2.1 ± 0.1
		Orange	Foreground	−3.7	0.5 ± 0.009	3.6 ± 0.10	6.9 ± 0.2
p-$H_2^{16}O$	33.9	Blue	Outflow	−19.7	0.2 ± 0.004	3.0 ± 0.06	18.9 ± 0.6
2_{02}–1_{11}		Green	Envelope	−7.7	0.4 ± 0.009	2.6 ± 0.08	6.4 ± 0.2
		Orange	Foreground	−3.7	0.3 ± 0.007	1.8 ± 0.040	13.1 ± 0.3
p-$H_2^{16}O$	39.6	Blue	Outflow	−19.7	0.1 ± 0.005	2.6 ± 0.20	23.5 ± 1.6
2_{11}–2_{02}		Green	Envelope	−7.7	0.2 ± 0.010	1.5 ± 0.10	6.8 ± 0.4
		Orange	Foreground	−3.7	0.1 ± 0.010	1.8 ± 0.20	14.4 ± 0.9
o-$H_2^{16}O$	39.0	Blue	Outflow	−19.7	0.1 ± 0.005	2.3 ± 0.20	23.2 ± 1.2
3_{12}–3_{03}		Green	Envelope	−7.7	0.2 ± 0.010	2.3 ± 0.90	9.3 ± 0.4
		Orange	Foreground	−3.7	0.09 ± 0.010	1.3 ± 0.30	12.5 ± 1.0
o-$H_2^{16}O$	39.9	Blue	Outflow	−19.7	0.2 ± 0.009	3.3 ± 0.20	16.7 ± 1.0
3_{12}–2_{21}		Green	Envelope	−7.7	0.2 ± 0.050	2.4 ± 0.40	9.9 ± 0.7
		Orange	Foreground	−3.7	0.2 ± 0.007	2.0 ± 0.20	11.5 ± 0.8
o-$H_2^{18}O$		Red	Envelope	−8.9 ± 0.2	0.02 ± 0.002	0.1 ± 0.03	4.0 ± 0.4
1_{10}–1_{01}	5.5	Cyan	Foreground	−3.3 ± 0.1	0.02 ± 0.004	0.03 ± 0.004	1.2 ± 0.2
p-$H_2^{18}O$	5.6	⋯	⋯	⋯	⋯	⋯	⋯
2_{02}–1_{11}		⋯	⋯	⋯	⋯	⋯	⋯
o-$H_2^{18}O$	4.9	⋯	⋯	⋯	⋯	⋯	⋯
3_{12}–3_{03}		⋯	⋯	⋯	⋯	⋯	⋯

Note. Gaussian components categorized by velocity and FWHM: all o-$H_2^{16}O$ central velocities fixed in value.

$H_2^{18}O$, constraints can be placed on these parameters. This is the ultimate goal.

RATRAN input models vary the following parameters as a function of radius: the density of an exciting collider (ortho and para H_2), the density of the molecule producing the observed spectral line (e.g., $H_2^{18}O$ or $H_2^{16}O$), temperature, and velocity field (ordered motion, e.g., infall $\boldsymbol{v}_r$, and turbulence $\boldsymbol{b}$). For a Gaussian line profile, the turbulence is related to the line width via

$$\frac{b}{\mathrm{FWHM}} = \frac{1}{2\sqrt{\ln 2}} = 0.60. \quad (1)$$

The density and temperature model was obtained from Crimier et al. (2010), who fitted a density power law $\rho \propto r^{-p}$, where $p = 1.4$; we confirmed this model via DUSTY (Ivezic et al. 1999), using the O&H Jena dust model. Water collision rates were obtained from Daniel et al. (2011) (H_2O–H_2) and input to RATRAN alongside the model file in order to generate energy level populations. This is unlike the majority of the previous IM studies; these studies instead used H_2O–He collision rates from Green et al. (1993), scaled by molecular mass to convert from collisions with helium to collisions with molecular hydrogen. The new collision cross sections (i.e., Daniel et al. 2011) are the result of directly modeling the molecular hydrogen collisions. At temperatures below 100 K the lowest energy transitions had very different cross sections, in some cases varying by a factor of four or five. In the absence of any collision rate data for $H_2^{18}O$ we instead used the $H_2^{16}O$ data, but of course modeled the $H_2^{18}O$ at much lower abundances (typically 1/550, Wilson & Rood 1994; Langer et al. 1984) than the $H_2^{16}O$.

Our analysis considers an abundance jump due to dust-grain water sublimation at 100 K. This divides the envelope into "inner" and "outer" regions. Our basic model used 22 increments with a central empty gap, with radii ranging from 95 to 18,600 au. These increments were spaced logarithmically (i.e., increment spacing closer together in the innermost regions). We tested models with a larger number of radial increments but did not find significant differences in the fundamental line parameters (line shape and width) although there were some slight changes in the line intensity.

The inner and outer radii of NGC 7129 FIRS 2 (0.08 ″ and 15 ″, respectively, see Table 1) do not fill the HIFI beam for any of the water emission lines (see Table 2), thus the modeled envelope is also smaller than the beam size. To remedy this, RATRAN output results were convolved with the emission line beamsizes (Roelfsema et al. 2012, Table 2) to produce a more accurate model of the observations.

This analysis allowed us to determine that these RATRAN models for water are not sensitive to any of the inner envelope parameters. Alternately, the model was most sensitive to the outer envelope abundance and turbulent velocity. This was not expected; it was known from previous work (e.g., Johnstone et al. 2010) that the ground-state lines only probe the outermost regions of the envelope. However, it was expected that $H_2^{16}O$ lines probing higher temperatures, or the low abundance isotopologue $H_2^{18}O$, would provide constraints on the inner envelope. Now, after an extensive exploration of model parameters, it is clear that this is not the case.

Our fitting procedure began with fitting the $H_2^{18}O$ 547 GHz emission. This line was simple in structure (well fitted by a Gaussian) and expected to be the lowest in optical depth and

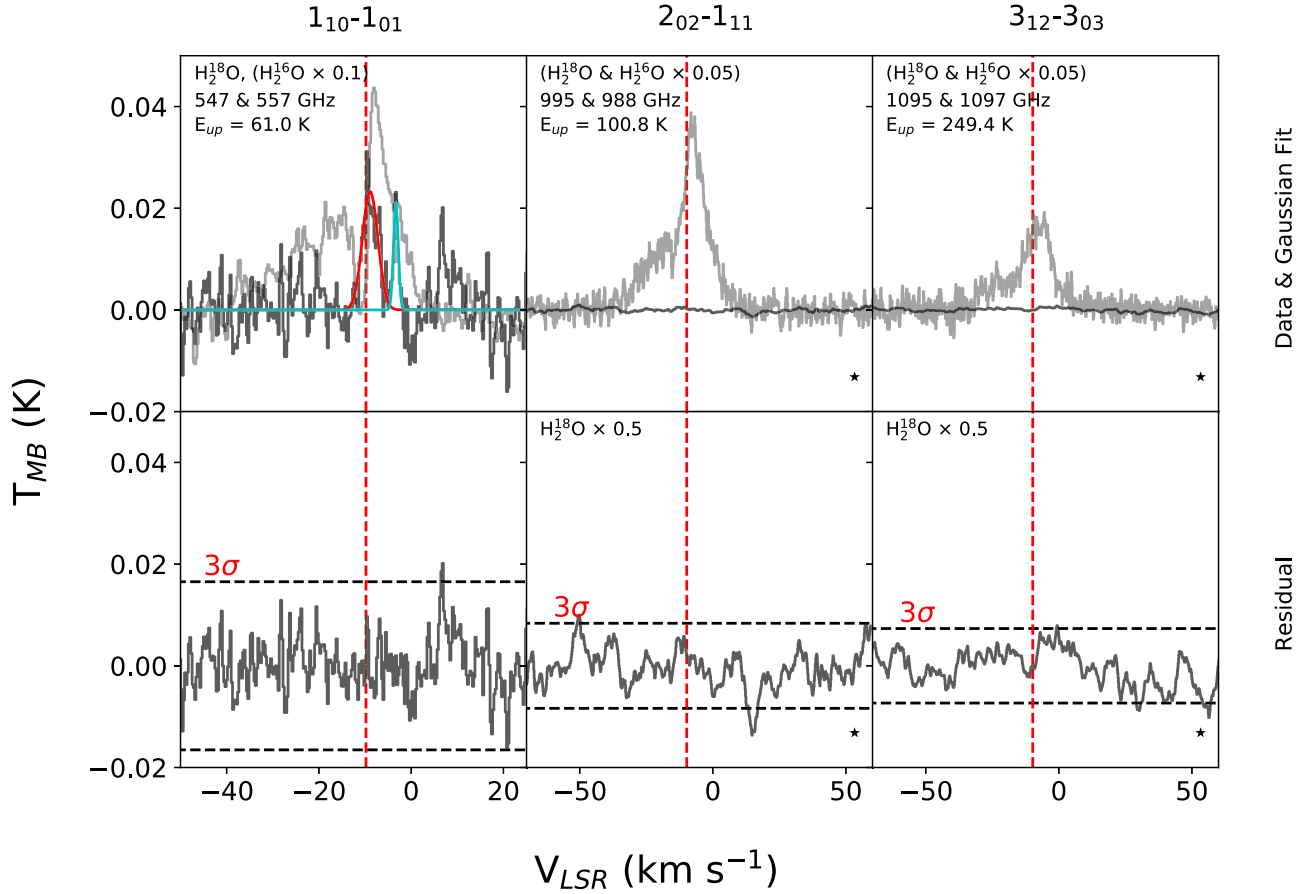

Figure 4. NGC 7129 FIRS 2: $H_2^{18}O$ Gaussian Fits contrasted with $H_2^{18}O$ (darker) and $H_2^{16}O$ (lighter) HIFI data. Narrow feature located at −8.9 km s^{-1} (red) and narrow feature at −3.36 km s^{-1} (cyan). See Table 3 for further details. Local V_{LSR} = −9.8 km s^{-1}. Gaussian fits are subtracted from the HIFI data, yielding the residuals in the bottom panels. The 3σ boundaries around the residuals represent the goodness of fit of the Gaussians. $H_2^{16}O$ lines are scaled by 0.1 (o001), and 0.05 (p002, o007), and $H_2^{18}O$ residuals (p002, o007) are scaled by 0.5.

therefore to sample most of the envelope. Models that gave a good fit to this line are scaled up in abundance and run for $H_2^{16}O$ emission lines and then compared to the appropriate Gaussian component. For $H_2^{16}O$, we compared the final resulting good fits to the total observed emission through a combination of visual inspection and chi-square calculations to ensure that our fits were appropriate, since the models themselves only occasionally produced Gaussian-like line profiles. The non-Gaussian profiles of some models occur at high optical depths.

A great many models were constructed to reproduce the $H_2^{18}O$ emission, spanning a large range of abundances and velocity fields (Table 4). The resultant fits to the HIFI data were compared through a chi-squared calculation. We tested a range of radial velocity fields including a constant infall velocity, a varying infall velocity, a freefall velocity, and an expanding velocity. We ruled out large constant infall and expanding velocities. The varying/freefall models fit the observational data the best. Ultimately, a freefall velocity toward a 1.1 $M_\odot$ was assumed. The velocity field for this varies from an infall velocity of 1 km s^{-1} at the outermost part of the envelope to 4.4 km s^{-1} at the inner edge. We compared our models using the Daniel et al. 2011 collision rates to models using Daniel et al. (2011) collision rates altered by 10% and determined that the spectral line results are very sensitive to the choice of collision rates. For example, increasing the collision rate by 10% increased the spectral line intensity by up to a factor of 4.5 for the 547 GHz line (ground-state o-H218O).

Table 4
Tested RATRAN Parameter Ranges

Parameter	Range	Unit
X_{out}	10^{-12}–10^{-10}	
X_{in}	10^{-8}–10^{0}	
b	0.5–4.0	km s^{-1}
v_r	−4.0–0.0, and FF[a]	km s^{-1}

Note.
[a] Freefall toward 1.1 $M_\odot$ central mass.

The final RATRAN model for $H_2^{18}O$ can be seen in Figure 5. The RATRAN model for $H_2^{18}O$ was multiplied by a range of abundance ratios ($X(H_2^{16}O)/X(H_2^{18}O)$ from 2 to 550) in order to find which best reproduced the HIFI observations of $H_2^{16}O$.

The $H_2^{16}O$ best-fit molecular lines can be found in Figure 6, obtained by modeling this molecule independent of $H_2^{18}O$. The 752, 1097, and 1153 GHz modeled lines fit the $H_2^{16}O$ envelope Gaussian components well, while the 988 GHz modeled line fits the envelope Gaussian well in terms of width and intensity, but not line shape. The asymmetrical line shape of the 988 GHz line does appear similar to that seen in the corresponding HIFI observations. The ground-state modeled lines do not fit the

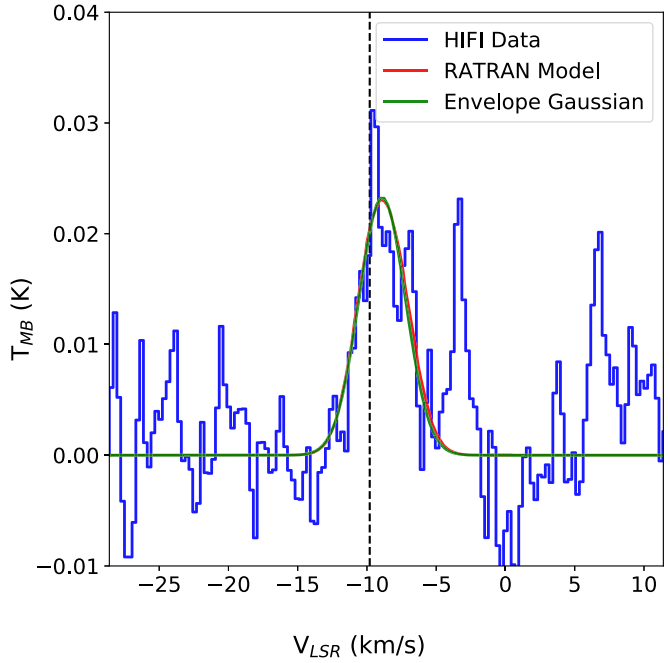

Figure 5. Final RATRAN model for $H_2^{18}O$ NGC 7129 FIRS 2. HIFI spectral observations (blue), the RATRAN spectral model (red), and the original red envelope Gaussian fit from Figure 4 (green). $V_{LSR} = 9.8$ km s^{-1} (dashed black).

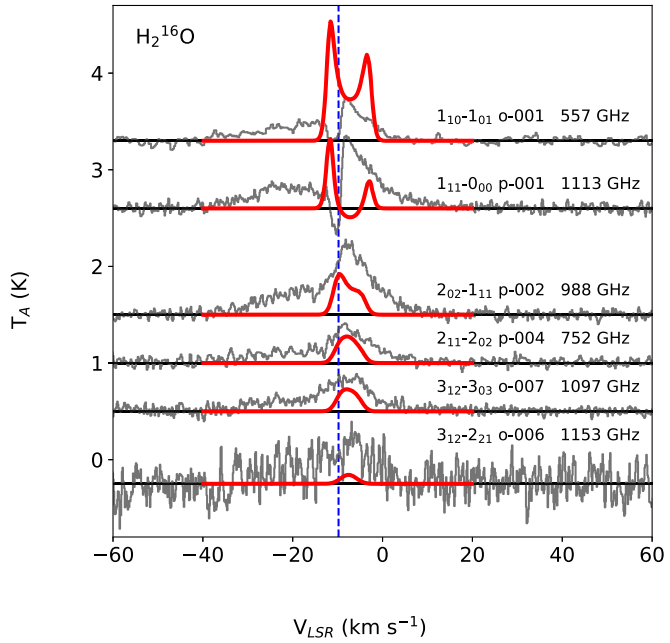

Figure 6. Final RATRAN model for $H_2^{16}O$ NGC 7129 FIRS 2. HIFI spectral observations (gray) and the RATRAN spectral model (red). $V_{LSR} = 9.8$ km s^{-1} (dashed blue). $X_{ratio} = 4.3 \pm 1.5 \times 10^2$.

Gaussian fits or the observations well at all. No single value for water abundance or turbulence gives ideal fits for all of the water lines simultaneously. The abundance ratio of $H_2^{16}O$ to $H_2^{18}O$ that produces these best fits is $X_{ratio} = 4.3 \pm 1.5 \times 10^2$.

We expected the velocity field parameters to be identical for $H_2^{18}O$ and $H_2^{16}O$. RATRAN models for both isotopologues appear to fit the HIFI observational data well enough, supporting this expectation.

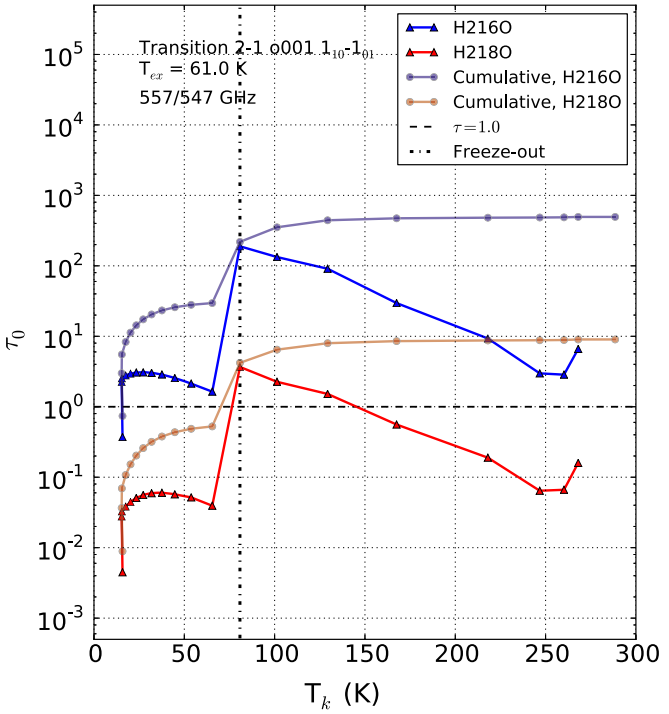

Figure 7. Ortho 001 (1_{10}–1_{01}): optical depth plotted against temperature. Triangles: red = $H_2^{18}O$ τ per RATRAN radial increment, blue = $H_2^{16}O$ τ per RATRAN radial increment; vertical green dashed = abundance drop radius, horizontal black dashed = $\tau = 1.0$. Circles: red = $H_2^{18}O$ cumulative τ, blue = $H_2^{16}O$ cumulative τ. The $H_2^{18}O$ o001 line becomes optically thick just inside the freeze-out radius ($T \sim 90$ K). The same line for $H_2^{16}O$ becomes optically thick almost immediately ($T \sim 15$ K). Maximum Optical Depth: $H_2^{16}O$ $\tau_{max} = 494.50$, $H_2^{18}O$ $\tau_{max} = 9.02$.

3.1. Optical Depth Study

Except for some extreme velocity field models that did not fit any of the data, none of our models showed any sensitivity to the parameters describing the inner envelope. The primary parameter of the inner envelope conditions is the abundance of the two isotopologues. The temperature and density structure is set by the dust emission studies (Crimier et al. 2010). In attempting to understand this result—especially the lack of sensitivity of the highest temperature probes among the $H_2^{16}O$ lines—we undertook a careful examination of the optical depth in each line in the best-fitting models.

We followed the optical depth calculations set out by van der Tak et al. (2007) and we developed a simple visualization tool capable of determining where the optical depth in a molecular line approaches 1 within a molecular cloud. We used the optical depth equation in the form:

$$\tau = \frac{A_{ul}}{8\pi\tilde{\nu}^3} \frac{N}{1.0645\Delta V} \left(f_l \left(\frac{g_u}{g_l} \right) - f_u \right) \quad (2)$$

and found the values for all of the parameters needed here in the data files provided with RATRAN. The data files used were the latest available for RATRAN at the time, acquired from the Leiden Atomic and Molecular Database (Schöier et al. 2005).

We constructed plots of optical depth in each water line, both incremental and total inwards from the outer radius. In Figure 7 we show a plot of these optical depths for the identical ground-state lines for both $H_2^{16}O$ and $H_2^{18}O$. The $H_2^{16}O$ ground-state line optical depth is optically thick almost immediately into the

Table 5
Envelope Temperature Where Optical Depth $\tau = 1$ for Each Water Line

Water	Line	T_k (K)	τ_{max}
$H_2^{16}O$	o001	15	495
	p001	15	494
	p002	38	204
	p004	54	309
	o006	90	62
	o007	80	342
$H_2^{18}O$	o001	90	9
	p002	168	1
	o007	100	4

Note. τ_{max} = maximum optical depth.

envelope (∼15 K), indicated by the dark blue line and triangular markers. Here, the markers indicate each of the RATRAN radial increments and the horizontal dashed line indicates where $\tau = 1$, marking the transition from optically thin to thick. The large optical depth accounts for the lack of $H_2^{16}O$ sensitivity to conditions deeper within the region as modeled by RATRAN. This transition is likely not an ideal probe of the envelope. The same line for $H_2^{18}O$ becomes optically thick near the freeze-out radius, at ∼90 K, indicated by the thick red line with triangular markers, and thus probes most of the outer envelope. Table 5 lists the temperature where the studied water transition becomes optically thick in the RATRAN models; the maximum optical depth is also listed. These show that all of the $H_2^{16}O$ lines become optically thick in the outer envelope, explaining why none are sensitive to conditions in the inner envelope.

Excited ortho-$H_2^{16}O$ lines and $H_2^{18}O$ lines are the more useful lines for modeling as they are optically thin until approximately the freeze-out radius; this allows the majority of the outer envelope to be modeled. Specifically, the $H_2^{18}O$ 995 GHz line (p002, $T_{ex} = 100.8$ K) is optically thin in the outer envelope, and reaches a modest maximum optical depth of $\tau = 1.23$. Although this line seems promising for probing the star formation region, this transition was observed but not detected in this work. Since this transition becomes optically thick around 167.5 K, the photons that RATRAN is using to model with originate from 129 to 15.8 K. The nondetection is partially explained by the beam dilution, which has a greater effect on the interior regions due to their smaller angular diameter. At this radius (∼0.578 ″), the beam dilution for this line is calculated to be $\sim 7.35 \times 10^{-4}$, assuming a beam size of 21.464 ″ (from Table 2).

The 995 GHz line could potentially be a good probe into the innermost radii of star formation regions assuming longer integration times are possible.

As for the other $H_2^{18}O$ transitions, the optical depth calculations suggest the o007 line (1095 GHz) would not be a good inner envelope probe for this particular star formation region (with maximum $\tau = 4.16$; optically thick at ∼100 K, the transition point of inner to outer envelope).

The optical depth calculations support that RATRAN is successfully modeling only the spectral contribution from the outer envelope. For a more in-depth discussion, please see Conrad (2018).

Table 6
RATRAN Best-fit Parameters for NGC 7129 FIRS 2

Molecule	Parameter	Value
o-$H_2^{18}O$	X_{out}	$3.5 \pm 0.3 \times 10^{-11}$
o-$H_2^{16}O$	X_{out}	$1.5 \pm 0.5 \times 10^{-8}$
p-$H_2^{16}O$	X_{out}	$4.5 \pm 0.5 \times 10^{-9}$
Total $H_2^{16}O$	X_{out}	$1.95 \pm 0.5 \times 10^{-8}$
	b	2.25 ± 0.25 km s^{-1}
$H_2^{18}O$	V_{inf}	Freefall,
&		-0.5 km s^{-1}
$H_2^{16}O$	OPR	3.3 ± 1.2
	X_{ratio}	$4.3 \pm 1.5 \times 10^2$

4. Discussion

4.1. Modeling Water in NGC 7129 FIRS 2

The extensive parameter investigation conducted with RATRAN for NGC 7129 FIRS 2 produced fruitful results for the outer envelope, but the inner envelope parameters were unable to be constrained. A primary initial goal of this work was to learn about the inner envelope and in this we have not been successful.

The inability to deduce a water abundance for the inner envelope of NGC 7129 FIRS 2 led us to investigate the optical depth of each line as a function of radius. We learned that even these excited state lines of $H_2^{16}O$ become optically thick in the outer envelope. The dividing point between inner and outer envelope was set at 100 K, the temperature where the abundance of water is expected to change abruptly by many orders of magnitude as it remains frozen at lower temperatures (i.e., the outer envelope) but sublimates at higher temperatures (i.e., the inner envelope). The higher excitation lines observed had excitation temperatures spanning the range of 101 to 249 K. However our analysis of the optical depths showed that all of these lines become optically thick in regions of much lower temperatures. In a few models with extreme velocity fields we found that emission from the inner envelope could reach the outside of the envelope but only in small amounts of emission in the wings of the main line. These models failed for other reasons (e.g., large self-absorption that is not seen in the data).

The best-fit values can be found in Table 6, showing abundances of each modeled water isotopologue, the velocity field, the OPR, and the $H_2^{16}O$ to $H_2^{18}O$ abundance ratio. For both water isotopologues, a turbulent velocity was determined to be $b = 2.25 \pm 0.25$ km s^{-1}. The models showing infall were preferred over stationary models with slightly better fits found for freefall toward a 1.1 $M_\odot$ central mass, or a constant infall of -0.5 km s^{-1}; considering the optical depth calculated, only the outer envelope velocities would have a significant effect on the modeled spectral line. These velocities are approximately equal for both best-fit cases considered, thus making it difficult to distinguish between the two.

Our final total water abundance in the outer envelope is 2.0×10^{-8}, an order of magnitude less than the value of $X_{out} = 3.3 \times 10^{-7}$ found by Johnstone et al. (2010) (with the out-dated data pipeline and collision rates).

4.2. Mass-regime Comparison of Abundance

The study of IM star formation is expected to bridge the knowledge gap between the high and LM regimes. In order to

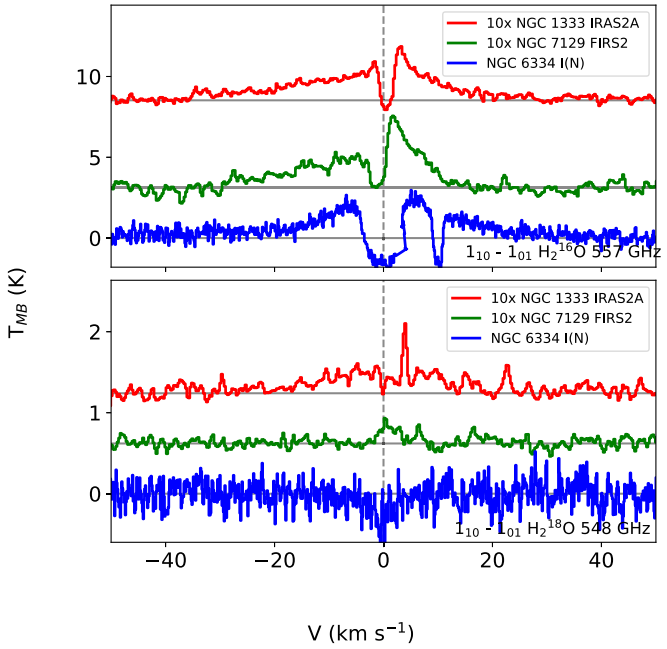

Figure 8. Comparing $H_2^{16}O$ and $H_2^{18}O$ spectra of three different sources observed with HIFI: NGC 1333 IRAS 2A (LM, red, scaled 10x), NGC 7129 FIRS 2 (IM, green, scaled 10x), and NGC 6334 I(N) (HM, blue). All spectra are positioned such that they align with 0 km s^{-1}.

determine how our IM study compares with that of the other regimes, we juxtapose a small sample of HM, IM, and LM spectra (Figure 8). Additionally, we compare best-fit physical envelope parameters that were obtained through radiative transfer modeling by multiple references (Table 7).

The ground-state ortho line for both isotopologues was compared between sources of all three mass regimes in Figure 8: a HM YSO NGC 6334 I(N) ($L_{\rm bol} = 1900\ L_\odot$, $d = 1700$ pc, $v_{\rm LSR} = -3.3$ km s^{-1}) (Sandell 2000; Neckel 1978), an IM YSO NGC 7129 FIRS 2 ($L_{\rm bol} = 430\ L_\odot$, $d = 1260$ pc, $v_{\rm LSR} = -9.8$ km s^{-1}; Shevchenko & Yakubov 1989; Johnstone et al. 2010), and a LM YSO NGC 1333 IRAS 2A ($L_{\rm bol} = 20\ L_\odot$, $d = 235$ pc, $v_{\rm LSR} = +7.5$ km s^{-1}) (Hirota et al. 2008; Kristensen et al. 2010). The $H_2^{16}O$ observation for NGC 6334 I(N) shows evidence of absorption by a foreground cloud $\sim(-3.3\ +)\ 10$ km s^{-1} (see Emprechtinger et al. 2013 for more on this). From this figure, it is clear that the particular sources chosen for LM and IM are very similar. In the top panel ($H_2^{16}O$), they have relatively similar intensities and line shapes, and have similar broad components probably attributed to the outflow. The HM source $H_2^{16}O$ line shape is very much stronger, with much broader and deeper absorption. The HM absorption is symmetrical about the local $V_{\rm LSR}$ axis, wider than the LM and IM counterparts, and saturated (i.e., dips below the continuum and flattens). Similar to the $H_2^{16}O$, the $H_2^{18}O$ luminosity and complexity of the spectra are similar for LM and IM.

We compare best-fit physical envelope parameters across mass regimes in Table 7. We include nine HM YSOs, two IM YSOs, and three LM YSOs. Mottram et al. (2013) study six LM YSOs in addition to the one recorded, but do not report their findings for these. Here, we compare the calculated envelope mass, the power-law density profile parameter p, the $H_2^{16}O/H_2^{18}O$ abundance ratio $X_{\rm ratio}$, turbulent velocity b, and the inner and outer envelope abundances of both isotopologues. The power-law parameter p ranges between 1.2 and 1.5 in the HM regime (with one outlier $p = 2.5$, IRAS 05358), between 1.35 and 1.4 in the IM, and between 1.5 and 1.8 in the LM. HM and IM YSOs appear to have more turbulent envelopes than LM. Most references assume an abundance ratio $X_{\rm ratio} = 500$; aside from this work, only Herpin et al. (2016) calculate actual abundance ratios with values ranging from 363 to 642. When possible, inner envelope $H_2^{16}O$ abundance calculations yielded a range of 0.1–14 $\times\ 10^{-5}$ across the mass regimes with an outlier of 60 $\times\ 10^{-5}$, derived by Mottram et al. (2013). Like us, Marseille et al. (2010) (HM), Johnstone et al. (2010) (IM), and Kristensen et al. (2010) (LM) did not constrain this value. All references constrained $H_2^{16}O$ in the outer envelope, yielding values on the order of 10^{-10}–10^{-7} across the mass regimes. The $H_2^{18}O$ inner abundance was constrained by Herpin et al. (2016) (HM), Chavarría et al. (2010) (HM), Herpin et al. (2012) (HM), Emprechtinger et al. (2013) (HM), and Mottram et al. (2013) (LM); the values range from 10^{-9} to 10^{-7} across the mass regimes. Finally, the $H_2^{18}O$ outer abundance was constrained by most references between 10^{-13}–10^{-10}. The water abundance values constrained in this work are consistent with those in both the high and LM regimes. The values found in Table 7.

Two references add an absorbing layer outside of the envelope when modeling to account for self-absorptions; Mottram et al. (2013) report outer envelope abundance values for both water isotopologues that are approximately an order of magnitude less than the rest of the sample, while the inner abundance values are greater on average. Coutens et al. (2012) report values that are more consistent with the rest of the sample. Both of these references report photodesorption layer water abundances on the same order of magnitude (10^{-7}).

The deduced turbulent velocity of this work (2.25 ± 0.25 km s^{-1}) is more consistent with that of the HM studies. The derived abundance ratio of $4.3 \pm 1.5 \times 10^2$ is consistent with the ratio $\sim$437 derived by Herpin et al. 2016 (HM).

5. Conclusions

We analyzed *Herschel* HIFI spectroscopy of water ($H_2^{18}O$ and $H_2^{16}O$) in the vicinity of NGC 7129 FIRS 2 using the radiative transfer code RATRAN. This appears to be one of the first thorough studies of the role of $H_2^{18}O$ in IM star formation regions.

For NGC 7129 FIRS 2, we assume a drop abundance-profile at the freeze-out radius ($T = 100$ K). We deduce an outer envelope $H_2^{16}O$ abundance of $1.95 \pm 0.5 \times 10^{-8}$ (ortho-H_2O + para-H_2O) m and ortho-$H_2^{18}O$ abundance of $3.5 \pm 0.3 \times 10^{-11}$. Inner abundances were not constrained. The turbulence was constrained to $2.25\ \pm 0.25$ km s^{-1}. We constrained the infall velocity to either a constant -0.5 km s^{-1} or freefall toward a central mass of $1.1\ M_\odot$. We calculate an OPR of 3.3 ± 1.2, and an $H_2^{16}O/H_2^{18}O$ abundance ratio of $4.3 \pm 1.5 \times 10^2$.

We also conducted an optical depth analysis; we found that the inner abundances were not able to be constrained due to the high opacities. This analysis also showed the spectral lines with the highest potential for successfully probing the star formation region are the excited $H_2^{18}O$ lines. This optical depth analysis proved to be a really useful tool in the modeling process.

Revisiting the RATRAN models of NGC 7129 FIRS 2 to include a photodesorption layer on the extremities of the outer

Table 7
Comparison of Water Abundance Calculations Across Mass Regimes

Reference	Regime	YSO	M_{env}	p	X_{ratio}	b (km s^{-1})	X_{in} ($H_2^{16}O$) (10^{-5})	X_{out} ($H_2^{16}O$) (10^{-8})	X_{PDL} ($H_2^{16}O$) (10^{-7})	X_{in} ($H_2^{18}O$) (10^{-8})	X_{out} ($H_2^{18}O$) (10^{-11})
[a]	HM	NGC 6334 I(N)	3826	1.3	437	2.5	0.4	2.3	⋯	0.9	5.3
	HM	W43-MM1	7550	1.5	⋯	Increasing	14	6.7	⋯	⋯	⋯
	HM	DR 21(OH)	472	1.35	531	2.5	0.5	14	⋯	0.9	26
	HM	IRAS 16272	2170	1.5	363	2.2	0.2	4.7	⋯	0.5	13
	HM	IRAS 05358	142	2.5	642	2	1.3	8.8	⋯	2.0	14
[b]	HM	W3 IRS5	250	1.2	500[A]	2.0	10	2	⋯	20	4.0
[c]	HM	W43-MM1	3520	1.5	450[A]	2.2–3.5	14	8	⋯	31	18
[d]	HM	NGC 6334 I(N)	3826	1.5	500[A]	3	0.1	0.3	⋯	0.2	0.6
[e]	HM	G31.41 + 0.31	1500	1.5	500[A]	1.4	⋯	3.1	⋯	⋯	6.2
	HM	G29.96-0.02	700	1.5	500[A]	1.1	⋯	0.05	⋯	⋯	0.1
	HM	W33A	4000	1.5	500[A]	1.6	⋯	0.06	⋯	⋯	0.1
	HM	W43-MM1	2000	1.5	500[A]	3.0	⋯	4.0	⋯	⋯	8.0
[f]	IM	NGC 7129 FIRS 2	50	1.4	550[A]	2.0	⋯	33	⋯	⋯	30
[g]	IM	Vela IRS 17	105	1.35	⋯	1.7	0.1–10	6.0	⋯	⋯	⋯
This work	IM	NGC 7129 FIRS 2	50	1.4	430	2.25	⋯	2.0	⋯	⋯	3.5
[h] LIME (Brinch & Hogerheijde 2010)	LM	NGC 1333 IRAS 2A	1	1.5	⋯	0.8	⋯	1.0	⋯	nd	nd
	LM	NGC 1333 IRAS 4A	4.5[i]	1.5	⋯	0.8	⋯	1.0	⋯	nd	nd
[j]	LM	IRAS 16293–2422	⋯	1.8	500[A]	0.3	0.5	1.5	1.3–5.3	1.0	3.0
[k]	LM	NGC 1333 IRAS 4A	5.2	1.8	500[A]	0.4	60	0.03	3.0	12	0.06

Notes. All references used RATRAN (except where indicated) and considered a freeze-out temperature of 100 K. (^{A}) = assumed abundance ratio. nd = model result not detectable. PDL = photodesorption layer.
[a] Herpin et al. (2016).
[b] Chavarría et al. (2010).
[c] Herpin et al. (2012).
[d] Emprechtinger et al. (2013).
[e] Marseille et al. (2010).
[f] Johnstone et al. (2010).
[g] Tisi (2013).
[h] Kristensen et al. (2010).
[i] Jørgensen et al. (2009).
[j] Coutens et al. (2012).
[k] Mottram et al. (2013).

envelope has potential to provide results more consistent with the observations.

HIFI has been designed and built by a consortium of institutes and university departments from across Europe, Canada and the United States under the leadership of SRON Netherlands Institute for Space Research, Groningen, The Netherlands and with major contributions from Germany, France and the US. Consortium members are: Canada: CSA, U. Waterloo; France: CESR, LAB, LERMA, IRAM; Germany: KOSMA, MPIfR, MPS; Ireland, NUI Maynooth; Italy: ASI, IFSI-INAF, Osservatorio Astrofisico di Arcetri-INAF; Netherlands: SRON, TUD; Poland: CAMK, CBK; Spain: Observatorio Astronómico Nacional (IGN), Centro de Astrobiología (CSIC-INTA). Sweden: Chalmers University of Technology—MC2, RSS & GARD; Onsala Space Observatory; Swedish National Space Board, Stockholm University—Stockholm Observatory; Switzerland: ETH Zurich, FHNW; USA: Caltech, JPL, NHSC.

ORCID iDs

Mollie E. Conrad https://orcid.org/0000-0002-6614-730X
Michel Fich https://orcid.org/0000-0002-5903-1886

References

Bechis, K. P., Harvey, P. M., Campbell, M. F., & Hoffman, W. F. 1978, ApJ, 226, 439
Bonnell, I. A., Bate, M. R., Clarke, C. J., & Pringle, J. E. 2001, MNRAS, 323, 785
Brinch, C., & Hogerheijde, M. R. 2010, A&A, 523, A25
Chavarría, L., Herpin, F., Jacq, T., et al. 2010, A&A, 521, L37
Cohen, M., & Kuhi, L. V. , 1979, ApJL, 227, L105
Conrad, M. 2018, $H_2^{18}O$ and $H_2^{16}O$ in Intermediate Mass Star Formation Regions. UWSpace, http://hdl.handle.net/10012/13855
Coutens, A., Vastel, C., Caux, E., et al. 2012, A&A, 539, A132
Crimier, N., Ceccarelli, C., Alonso-Albi, T., et al. 2010, A&A, 516, A102
Daniel, F., Dubernet, M.-L., & Grosjean, A. 2011, A&A, 536, A76
de Graauw, T., Helmich, F. P., Phillips, T. G., et al. 2010, A&A, 518, L6
Edwards, S., & Snell, R. L. 1983, ApJ, 270, 605
Eiroa, C., Palacios, J., & Casali, M. M. 1998, A&A, 335, 243
Emprechtinger, M., Lis, D. C., Rolffs, R., et al. 2013, ApJ, 765, 1
Evans, N. J., Dunham, M. M., Jørgensen, J. K., et al. 2009, ApJS, 181, 321
Font, A. S., Mitchell, G. F., & Sandell, G. 2001, ApJ, 555, 950
Fuente, A., Neri, R., & Caselli, P. 2005, A&A, 444, 481
Fuente, A., Neri, R., Martin-Pintado, J., et al. 2001, A&A, 366, 873
Fuente, A., Ceccarelli, C., Neri, R., et al. 2007, A&A, 468, L37
Green, S., Maluendes, S., & McLean, A. D. 1993, ApJS, 85, 181
Hartigan, P., & Lada, C. J. 1985, ApJS, 59, 383

Herpin, F., Chavarría, L., van der Tak, F., et al. 2012, A&A, 542, A76
Herpin, F., Chavarría, L., Jacq, T., et al. 2016, A&A, 587, A139
Hirota, T., Bushimata, T., Choi, Y. K., et al. 2008, PASJ, 60, 37
Hogerheijde, M. R., & van der Tak, F. F. S. 2000, A&A, 362, 697
Ivezic, Z., Nenkova, M., & Elitzur, M. 1999, User Manual for DUSTY. https://github.com/ivezic/dusty/blob/master/releaseV2/Manual/manual.pdf
Johnstone, D., Fich, M., McCoey, C., et al. 2010, A&A, 521, L41
Jørgensen, J. K., van Dishoeck, E. F., Visser, R., et al. 2009, A&A, 507, 861
Kristensen, L. E., Visser, R., van Dishoeck, E. F., et al. 2010, A&A, 521, L30
Langer, W. D., Graede, T. E., Frerking, M. S., & Armentrout, P. B. 1984, ApJ, 277, 581
Marseille, M. G., van der Tak, F. F. S., Herpin, F., et al. 2010, A&A, 521, L32
Matuszak, M., Karska, A., Kristensen, L. E., et al. 2015, A&A, 578, A20
McKee, C. F., & Tan, J. C. 2003, ApJ, 585, 850
Miranda, L. F., Eiroa, C., & Gómez de Castro, A. I. 1993, A&A, 271, 564
Mottram, J. C., van Dishoeck, E. F., Schmalzl, M., et al. 2013, A&A, 558, A126
Neckel, T. 1978, A&A, 69, 51
Neri, R., Fuente, A., Ceccarelli, C., et al. 2007, A&A, 468, L33
Ossenkopf, V., & Henning, T. 1994, A&A, 291, 943
Ott, S. 2010, in ASP Conf. Ser. 434, Astronomical Data Analysis Software and Systems XIX, ed. Y. Mizumoto, K.-I. Morita, & M. Ohishi (San Francisco: ASP)
Pilbratt, G. L., Riedinger, J. R., Passvogel, T., et al. 2010, A&A, 518, L1
Roelfsema, P. R., et al. 2012, A&A, 537, A17
Sandell, G. 2000, A&A, 358, 242
Schöier, F. L., van der Tak, F. F. S., van Dishoeck, E. F., & Black, J. H. 2005, A&A, 432, 369
Shevchenko, V. S., & Yakubov, S. D. 1989, SvA, 33, 370
Shu, F. H., & Adams, F. C. 1987, in IAU Symp. 122, Circumstellar Matter, ed. I. Appenzeller & C. Jordan (Dordrecht: Reidel), 7
Tan, J. A., Beltrán, M. T., Caselli, P., et al. 2014, Protostars and Planets VI, ed. H. Beuther et al. (Tucson, AZ: Univ. Arizona Press), 149
Testi, L., & Sargent, A. I. 1998, ApJL, 508, L91
Tisi, S. 2013, A Herschel/HIFI study of Water in Two Intermediate-Mass Star-forming Regions: Vela IRS 17 and Vela IRS 19 UWSpace, http://hdl.handle.net/10012/7594
van der Tak, F. F. S., Black, J. H., Schöier, F. L., et al. 2007, A&A, 468, 627
van Dishoeck, E. F., et al. 2011, PASP, 123, 138
Wilking, B. A., & Lada, C. J. 1983, ApJ, 274, 698
Wilson, T. L., & Rood, R. 1994, ARA&A, 32, 191
Wolfire, M. G., & Cassinelli, J. P. 1987, ApJ, 319, 850